Volume 3
Number 6
November 2025
Pages 1171–1410

EES Catalysis

rsc.li/EESCatalysis

ISSN 2753-801X

ROYAL SOCIETY OF CHEMISTRY

PAPER

Abdelaziz Gouda, Geoffrey Ozin *et al.*
Photofluidized bed reactor maximizes photon utilization in heterogeneous photocatalysis: theory to practice

EES Catalysis

PAPER

View Article Online
View Journal | View Issue

Cite this: *EES Catal.*, 2025, 3, 1246

Photofluidized bed reactor maximizes photon utilization in heterogeneous photocatalysis: theory to practice†

Haojin Wu,‡[ab] Abdelaziz Gouda,‡*[a] Shiquan Shan,[b] Zhijun Zhou[b] and Geoffrey Ozin*[a]

Scaling up gas-phase heterogeneous photocatalysis requires the development of high-efficiency, cost-effective photoreactors that maximize photon capture while minimizing parasitic light losses. The integration of photocatalysis with fluidized bed technology enhances light penetration, improves particle–light interactions, and facilitates mass and heat transfer. To elucidate the mechanisms behind enhanced light absorption in a photofluidized bed reactor (PFBR), we employed CFD-DEM simulations and ray tracing to model the absorption characteristics of fluidized particles. Compared to fixed-bed systems, fluidized beds demonstrated significantly improved light absorption, particularly for particles with lower intrinsic absorptivity. The effects of particle size and gas flow rate on light absorption were also analyzed. Experimental validation was conducted using a solar-driven reverse Boudouard reaction, demonstrating the photochemistry of fluidized carbon particles in a carbon dioxide flow within an annular quartz tube reactor, and facilitating carbon monoxide production. At experimentally low gas flow rates, the PFBR exhibited enhanced photocatalytic performance. Furthermore, a comparative analysis of thermochemical and photochemical performance between fluidized and fixed beds highlighted the remarkable solar advantages of PFBRs. The results underscore the advantages of fluidized bed reactors in achieving uniform mixing of reactant gases, particles, and light under isothermal, isobaric, and isophotonic reaction conditions, demonstrating their potential for scalable solar-driven catalytic processes.

Received 28th January 2025,
Accepted 16th May 2025

DOI: 10.1039/d5ey00023h

rsc.li/eescatalysis

Broader context

The transition to sustainable energy systems demands innovative technologies that optimize resource efficiency, including in the realm of photocatalysis for chemical transformations. Photoreactor design plays a critical role in maximizing photon utilization and minimizing energy losses, bridging fundamental research with scalable industrial applications. The development of advanced photofluidized bed reactors (PFBRs) represents a pivotal step toward achieving isothermal and isophotonic conditions for enhanced reaction efficiency. This work aligns with global efforts to integrate light-driven processes into renewable energy systems, offering transformative solutions for solar fuels, carbon management, and chemical production.

1. Introduction

As society develops and industrialization advances, environmental issues have emerged as one of the most pressing global challenges that require urgent attention.[1,2] Photocatalysis and photothermal catalysis, allow for the direct conversion of solar energy into chemical energy in the form of commodity chemicals and fuels, making it a valuable method for utilizing renewable energy sources.[3–5] Numerous studies focus on developing photocatalysts for applications such as water splitting,[6] CO_2 hydrogenation,[7] and methane dry reforming.[8] Beyond the pursuit of highly efficient photocatalysts, innovative engineering approaches to reactor design also play a significant role in enhancing the efficiency of solar-to-chemical conversion.[9,10]

Various types of reactors have been reported for photocatalysis or photothermal catalysis, including slurry-type reactors,

[a] Solar Fuels Cluster, Department of Chemistry, University of Toronto, 80 Saint George Street, Toronto, ON, M5S 3H6, Canada. E-mail: Abdelaziz.gouda@utoronto.ca, g.ozin@utoronto.ca
[b] State Key Laboratory of Clean Energy Utilization, Zhejiang University, Hangzhou, 310027, China

† Electronic supplementary information (ESI) available. See DOI: https://doi.org/10.1039/d5ey00023h

‡ Authors contributed equally to this work.

fixed bed reactors (FBR), structured reactors and so on.[11] The slurry-type reactor is commonly used due to its convenience; however, its development is limited by low light utilization.[12,13] In fixed-bed reactors, catalysts are placed on fixed supports that directly absorb light,[14–16] but only the top layer of the catalyst can be accessed by both light and the chemical feedstock. Structured reactors, commonly referred to as monoliths, have distinct shapes that incorporate numerous channels and a large surface area.[17–20] Avargani *et al.* analyzed a solar-driven porous bed catalytic reactor *via* simulations and experimental validation, achieving 62.93% propane conversion under optimized conditions during day–night operation.[21] Cao *et al.* designed a glass-waveguide-based ''shell-and-tube'' type photothermal reactor to increase the contact area between the catalyst and the light.[20] Mu *et al.* used a foam reactor to prevent uneven temperature distribution and severe carbon deposition during solar-driven CO_2 reformation of CH_4.[22] Kant *et al.* presented a low-cost, structured photoreactor for efficient solar-driven conversion of CO_2 and water into sustainable resources, with optical modelling guiding design to overcome efficiency and cost barriers.[23] This type of reactor enhances the contact area between the catalyst and the light, but it tends to have a complex structure. There is a significant research gap in developing scalable photoreactors with simple structures that can simultaneously enhance light transport and utilization while maximizing the interaction between catalysts and reactants.

The fluidized bed reactor is commonly used in thermal chemistry applications such as biomass gasification,[24–26] methane catalytic decomposition,[27–29] and coal combustion.[30,31] It has rarely been applied in photocatalysis or photothermal catalysis, with only a few initial attempts having been made.[32–35] Fluidized bed reactors offer several advantages, including uniform temperature distribution, excellent heat transfer performance, well-mixed reactants, and robust scalability for chemicals and fuels production at various scales.[36–38] By integrating fluidized bed technology into photocatalysis, the contact between catalytic particles and light can be significantly enhanced, which in turn improves the efficiency of light utilization.[39] Additionally, the characteristics of fluidized beds enhance heat and mass transfer, as well as temperature uniformity within the reaction system. This attribute makes the possibility of large-scale industrial applications of photocatalysis more feasible.[40,41] *Via* integration of photocatalysis and fluidized bed reactors, referred to as photofluidized bed reactors (PFBR), the challenges associated with scalable photocatalysis can be overcome. Therefore, PFBR is poised to play a significant role in the production of solar-driven chemicals and fuels, contributing meaningfully to sustainable energy conversion technologies of the future. A bench-scale annular fluidized-bed photoreactor with TiO_2-coated silica beads was proposed demonstrating optimized photocatalytic efficiency for phenol mineralization.[42] Reilly *et al.* used UV light to irradiate a fluidized bed reactor to drive Pt–TiO_2 to split water, increasing hydrogen production by optimizing gas–liquid mass transfer and flow control.[43] A novel fluidized bed reactor using Pt–TiO_2 spheres in sodium carbonate solution under UV light led to boosted hydrogen production by 44% to 211 μmol h^{-1}, attributed to better gas separation and reduced reverse reactions.[44] Lu *et al.* employed the Lagrangian multiphase particle-in-cell (MP-PIC) modelling was used to investigate CO_2 photoreduction in a gas–solid annular fluidized bed photoreactor, revealing maximum radiation intensity at the mid-reactor height and photocatalytic reactions near the inner wall, guiding reactor design and process optimization.[45] Bueno *et al.* demonstrated a high-efficiency fluidized bed photoreactor using TiO_2-coated borosilicate glass beads and high-radiance ultraviolet light-emitting diodes (UV-LEDs), achieving complete *n*-hexane oxidation *via* optimized catalyst loading and irradiation.[46] Current research on PFBRs primarily focuses on verifying the ability of fluidized beds to enhance photocatalytic reactions solely through simulations and/or experiments. However, the underlying mechanisms have yet to be thoroughly explored from a microscopic perspective.

This work aims to explore the advantages of a PFBR in terms of light utilization and its enhancement of photocatalytic reaction processes through both simulations and experiments. Different from other studies on a fluidized bed reactor with light,[47] we utilized a two-phase flow model in conjunction with a ray tracing model to investigate the light absorption characteristics of the PFBR for the first time compared to a fixed-bed reactor. Our group has experimentally demonstrated a room-temperature, light-driven reverse Boudouard process ($C + CO_2 \rightarrow 2CO$) in a fixed bed reactor, which showed excellent performance.[48] This study presents the first demonstration of the reverse Boudouard photocatalytic reaction in a PFBR, highlighting its enhanced light utilization and improved reaction efficiency. By coupling the reverse Boudouard reaction with solar energy, this work introduces a novel pathway for carbon photochemical conversion. The PFBR architecture is particularly well-suited for photocatalytic systems involving low-absorptivity catalysts, and its structurally simple, scalable design offers a promising route toward industrial-scale photocatalytic applications.

2. Methods

The gas–solid two-phase motion in the fluidized state is solved by using the Euler–Lagrange approach.[49] The gas phase is treated as a continuous and fully interpenetrating phase based on the Euler method.[50] Newton's second law is used to solve the motion trajectory of each particle in the solid phase. When the gas flow passes through the particles, it exerts a force on the particles, thereby exchanging momentum with the particles, and the motion between the gas and solid phases is coupled. At the same time, in the fluidized bed, the concentration of solid particles is very high, and the accumulation of particles and mutual collision are inevitable. The discrete element method (DEM) model is used to calculate the movement and rotation of particles caused by the collision between particles, making the trajectory of particles in the airflow closer to the real situation.[51] The gas–solid two-phase flow dynamics within the

PFBR are simulated using a coupled CFD–DEM model, enabling precise tracking of individual particle positions. Ray tracing is then employed to analyze the interaction of incident light with the fluidized reaction zone, providing insights into light utilization efficiency.[52]

Scheme 1 illustrates the computational workflow for the PFBR. Firstly, the natural sedimentation process of a certain number of particles is simulated to form the initial state of the particles in the reactor. It can also be considered as a packed bed state. With the initial stationary position of the particles, CFD can get the velocity, pressure, and temperature with calculated volume fraction and momentum source. Then the drag force on the particle and particle collision is calculated sequentially. As the DEM iteration converges, particle positions and velocities are updated. These updated conditions are then used to recalculate the local volume fraction and momentum source terms, enabling the next cycle of the simulation to proceed until all time steps are completed. Using the particle positions at each time step, ray tracing is employed to evaluate the utilization efficiency of incident photons within the reactor.

It is worth noting that CFD-DEM simulations are widely applied in fluidized bed studies and have been extensively validated for their accuracy in capturing particle–fluid interactions. Munck *et al.* used the CFD-DEM method to simulate the particle drying process in a fluidized bed, and the simulation results were in good agreement with the experimental results.[53] Wang *et al.* coupled the CFD-DEM model with a heat exchange model, and the mixed model was validated for a pseudo-2D bubbling fluidized bed.[54] Liu *et al.* validated that the CFD-DEM model can accurately predict key fluidized bed parameters, including the mean and fluctuation frequency of bed pressure drop, minimum fluidization velocity, and time-averaged vertical particle velocity.[55] Additionally, the ray tracing method is widely employed in photoreactor simulations, where both the intensity and spatial distribution of rays can be experimentally validated.[52,56] In this work, only the light absorption characteristics of the particle bed are considered, while light intensity and energy exchange are not included in the analysis.

2.1 CFD model

The gas phase in the CFD model is considered as a continuous phase, and it can be described by using the Euler approach.[57] The mass and momentum conservation equations are as follows:

$$\frac{\partial}{\partial t}\left(\alpha_g \rho_g\right) + \nabla \cdot \left(\alpha_g \rho_g \vec{u}_g\right) = 0 \tag{1}$$

$$\begin{aligned}\frac{\partial}{\partial t}\left(\alpha_g \rho_g \vec{u}_g\right) + \nabla \cdot \left(\alpha_g \rho_g \vec{u}_g \vec{u}_g\right) \\ = -\alpha_g \nabla P + \nabla \alpha_g \cdot \tau_g + \alpha_g \rho_g g + F_{p-g}\end{aligned} \tag{2}$$

where, subscript g denotes the gas phase, α is the volume fraction, ρ is density, u is velocity, p is gas pressure, τ is stress tensor, g is the acceleration due to gravity, F_{p-g} is the source term for momentum, representing the interaction between particle and fluid. The k–ε mixture turbulence model is used for calculating the gas phase turbulence.

2.2 DEM model

The DEM model is used to describe particle motion, and the particle motion includes two states of motion: translational motion and rotational motion. Newton's second law is used to solve these two motions, and the models are shown below:

$$m_i \frac{\mathrm{d}u_i}{\mathrm{d}t} = F_{f,i} + m_i g + F_{c,i} \tag{3}$$

$$I_i \frac{\mathrm{d}\omega_i}{\mathrm{d}t} = \boldsymbol{T}_i \tag{4}$$

where, m_i is the mass of the particle, u_i is the velocity of the particle, $m_i g$ is the gravitational force, $F_{f,i}$ and $F_{c,i}$ are the

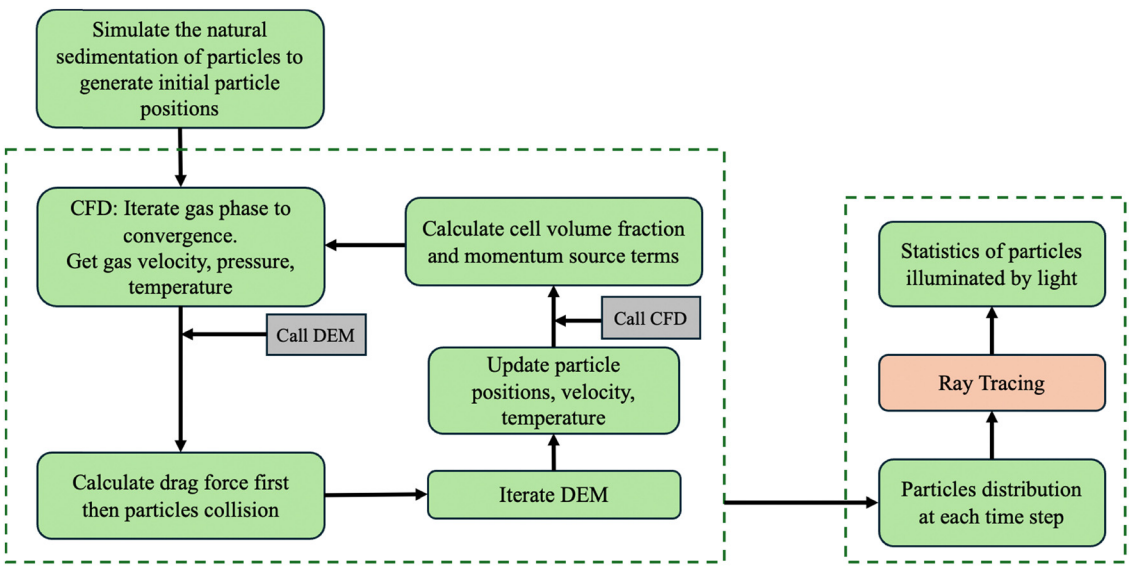

Scheme 1 Simulation workflow for the PFBR.

fluid force on the particles and the contact force between particles, respectively. ω_i is the particle's angular velocity, $\boldsymbol{T}_i$ is the torque, I_i is the moment of inertia. The Hertz–Mindlin (no slip) model[58] is used to solve particle contact force. The fluid force on the particles $F_{f,i}$ includes the fluid pressure gradient force on the particles $\boldsymbol{F}_{f,\nabla p}$ and the fluid drag force received by particles $\boldsymbol{F}_{d,i}$.

$$\boldsymbol{F}_{f,\nabla p} = -V_i \nabla p \tag{5}$$

$$\boldsymbol{F}_{d,i} = \alpha_i \frac{\beta}{1-\alpha_g}(\boldsymbol{u}_g - \boldsymbol{u}_i) \tag{6}$$

where V is the volume of particle i, ∇p is the fluid pressure gradient, and β is the momentum exchange coefficient between phases, which is calculated using the Gidaspow drag model:[59]

$$\beta = \begin{cases} \frac{3}{4} C_D \frac{\alpha_g \rho_g \alpha_i |\boldsymbol{u}_g - \boldsymbol{u}_i|}{d_i} \alpha_g^{-2.65} & \alpha_g \geq 0.8 \\ \frac{150\alpha_i(1-\alpha_g)u_g}{\alpha_g^2 d_i^2} + \frac{1.75\alpha_i \rho_g |\boldsymbol{u}_g - \boldsymbol{u}_i|}{\alpha_g + d_i} & \alpha_g < 0.8 \end{cases} \tag{7}$$

where α_i is the particle volume fraction, d_i is the particle diameter, and C_D is the drag coefficient. C_D can be calculated as follows:

$$C_D = \begin{cases} \frac{24}{Re_i}(1 + 0.15 Re_i^{0.687}) & Re_i < 1000 \\ 0.44 & Re_i \geq 1000 \end{cases} \tag{8}$$

where Re_i is the Reynolds number, which can be expressed as follows:

$$Re_i = \frac{\alpha_g \rho_g |\boldsymbol{u}_g - \boldsymbol{u}_i| d_i}{\mu_g} \tag{9}$$

where μ_g is the gas dynamic viscosity.

2.3 Ray tracing

The light source surrounds the fluidized reaction zone and provides photons for the catalytic reaction. The ray tracing model assumes that the geometry's size is much larger than the wavelength of light, and that there are no diffraction effects in the calculation, ignoring the wave nature of light. The light is emitted perpendicularly from the light source into the reaction tube. The particle surfaces are modelled as accumulators to calculate the total number of rays received by the particles' surface meshes and the light's intensity. Due to the small particle size, transmissive radiation through the particle has been neglected thus, the sum of absorptivity and reflectivity of the particle surface is 1.

The reflected ray might be absorbed by other particles or lost. To save computational resources, an intensity threshold of 1 mW m^{-2} was set for the reflected ray to avoid too many reflections by one ray. Since the reaction was carried out at atmospheric pressure, the mesh-free outer regions between the particles were assumed to be in a vacuum, rendering the light distribution independent of fluid dynamics.

2.4 Boundary conditions

Appropriate boundary conditions were essential for ensuring the accuracy of the CFD-DEM simulations. The reactor was filled with CO_2, introduced from the bottom of the reaction tube. Simulations were conducted at 773 K, with gas flow rates converted to standard conditions. A velocity inlet and pressure outlet were defined, with no-slip conditions at the reactor walls, and no heat exchange was considered. The total particle mass was 10 mg. Initial particle positions and bed height were determined *via* natural sedimentation. DEM collision parameters between particles and walls were based on their material properties. In the COMSOL ray tracing simulations, the particle surface absorptivity was assigned as required, and the inner wall reflectivity of the reactor was set to 0.05. A summary of all boundary conditions and simulation parameters is provided in Table 1.

2.5 Solution method

The structure of the reactor was constructed in ANSYS' Space Claim Software and meshed using ICEM. The reactor tube was modelled with an inner diameter of 4 mm and height of 100 mm. The reactor was simulated using an unstructured mesh. CFD-DEM simulation required the CFD mesh to be larger than the particle size, and to calculate the flow field accurately, the general mesh size had to be 3–4 times the particle size. Based on this, when simulating the particle flow of 110 μm, 200 μm and 300 μm particles, the number of mesh elements was 38 400, 4800 and 1200, respectively. The initial state of the particles in the reactor was obtained by simulating the natural settling of the particles using the Altair EDEM software until each particle velocity reached 0 m s^{-1}, then the CFD-DEM model was applied by coupling Ansys Fluent and EDEM software. These two software programs ran alternately to obtain the particle status. The calculation time step in Fluent was an integral multiple of that in EDEM, set to 1×10^{-4} s and 1×10^{-6} s, respectively. After the CFD-DEM calculation, the

Table 1 Boundary conditions and settings for simulations

Parameter	Value
Gas phase (CO_2)	
Density	Varies with temperature
Viscosity	Varies with temperature
Inlet gas flow	5, 10, 15 sccm
Particle phase	
Particle mass	10 mg
Particle diameter	110
Particle density	265 kg m^{-3}
Particle absorptivity	0.95
Simulation settings	
Restitution coefficient	0.5
Static friction coefficient	0.5
Rolling friction coefficient	0.01
Poisson's ratio of particle	0.28
Young's modulus of particle	31×10^6 Pa
Poisson's ratio of wall	0.25
Young's modulus of wall	5.5×10^7 Pa
Operation temperature	773 K

particle state and positions at every time step can be obtained. Using the particle position data, COMSOL Multiphysics with MATLAB was used to create geometry using MATLAB code in COMSOL Multiphysics. The wall thickness of the quartz tube was 1 mm. The initial height of the fixed bed containing 10 mg of 110 μm particles was 4.9 mm. For consistency, the length of the light source in both the fixed and fluidized bed configurations was set equal to this bed height. Accordingly, in the fluidized bed simulations, only the light absorption by particles within the bottom layer, corresponding to the fixed bed height, was considered. Geometrical Optics Physics in COMSOL Multiphysics was selected to simulate ray tracing. Due to limited computing resources, the light rays are only released from a line segment source parallel to the wall of the reaction tube, with the direction of the incident light perpendicular to the wall of the reaction tube. The total number of released rays was 1000. In COMSOL Multiphysics, the particle surface was defined as a ''Wall'', the surface boundary was set to ''Diffuse scattering'', and the surface of the quartz tube was set to ''Material discontinuity''. The total light utilization by the fluidized bed and fixed bed is calculated by the total power absorbed by the particle surfaces. COMSOL's ''Free tetrahedral'' meshing method was used since it is flexible enough to accommodate complex 3D geometries, with the maximum and minimum element sizes set to 5.5×10^{-4} and 1.8×10^{-5}, respectively.

2.6 Experimental setup

The reverse Boudouard reaction plays a crucial role in industrial processes such as coal gasification for syngas production and metallurgical applications.[60,61] Traditionally, part of the coal is combusted to generate the heat and carbon dioxide needed to sustain the reaction. However, this high-temperature process presents challenges, including ash melting and tar contamination.[62] By leveraging solar energy to drive this reaction directly, reliance on coal combustion can be significantly reduced. A light-driven process at room temperature minimizes the need for high-temperature heat, offering a more sustainable alternative. This reaction process can convert the CO_2 to be converted into solar fuel, which is of great significance for the world's energy conservation and emission reduction. Additionally, PFBR technology enhances light absorption and improves solar energy utilization, making it a promising approach for optimizing reaction performance and raw material efficiency. Given its industrial significance, the reverse Boudouard reaction has been selected as a model system to experimentally validate the PFBR's potential for large-scale applications.

The PFBR experimental setup included a 300 W Xenon lamp as the light source, with its spectral intensity distribution provided in Fig. S1 (ESI†), a quartz tube with 4 mm inner diameter, 6 mm outer diameter and 300 mm height, and a vibration motor as shown in Fig. 1. Carbon black (Vulcan XC72, Fuel cell) was sieved between 120 and 150 mesh sieves (diameter range: 106 μm to 120 μm). The tube was filled with 0.5 g of quartz sand with a diameter of 0.38–0.5 mm to make the airflow more uniform. 10 mg of carbon black was loaded

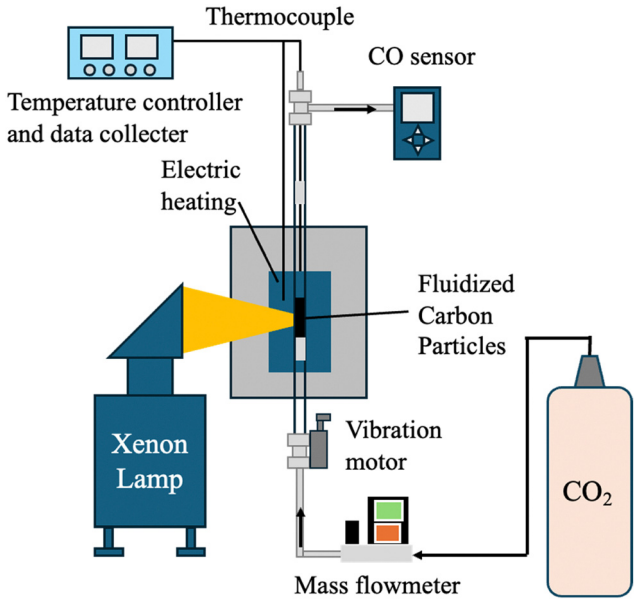

Fig. 1 Illustration of the experimental setup of the PFBR.

above the quartz sand. Since the carbon black has a very low density (265 kg m^{-3}), it is easy to form airflow channels during the fluidization process, thus stopping the fluidization state. Therefore, a vibration motor is tied to the bottom of the reaction tube to disrupt channelling (Videos S1 and S2, ESI†). Without the use of a vibration motor, the fluidized bed reactor required a higher gas flow rate for better fluidization of the particles. Higher gas flows lead to a waste of gas feedstock and significantly reduce the concentration of the product. One xenon lamp with a spot diameter of 5 mm was used to irradiate the particles from one side. Pure carbon dioxide gas (99.9% purity and purchased from Praxair) was used to both fluidize and react with the carbon particles. The generated CO is monitored and recorded using a CO sensor (Hengyang Peichen Electronic Commerce Co., Ltd (ANPIGGYCA-1), Detection range: 0–1000 ppm and CO accuracy: ±5%). The fixed bed reaction conditions were the same as those of the fluidized bed, except that in the fixed bed, the carbon particles were fixed in the middle by quartz sand. The temperature of the particles was accurately measured using a thermocouple that was carefully immersed within the particle system. A homemade electrical heating system surrounded the reaction tube, providing the thermal energy required for thermal reactions or light-assisted reactions. The temperature of the electrical heating system was also measured by another thermocouple. An OMEGA temperature controller was configured to regulate the temperature of particles and the reactor. This setup allowed for precise readings of the thermal properties of the particles, ensuring that the measurements reflected the actual temperature of the material *in situ*.

2.7 Characterization of carbon particles before and after the reaction

Carbon particles before and after the reaction were characterized using X-ray diffractometer (Bruker D2-Phaser using Cu Ka

radiation at 30 kV) and their morphologies were examined under transmission electron microscopy (Hitachi HF-3300). X-Ray photoelectron spectroscopy (XPS) results were extracted from Thermo Scientific Kα with an Al Kα X-ray source and the procedure was performed before and after the tests.

3. Results

3.1 The light absorption enhancement of the PFBR

The flow of particles in the PFBR in the gas flow is shown in Fig. 2. The particles were fluidized in the reactor, and the bed height was increased from the initial 4.9 mm to 20.5 mm. As a result, the distance between particles increased, and more particles floated in the reactor instead of accumulating. When the reactor bed was irradiated, due to the large spacing between particles, more light could penetrate deep into the reactor instead of being reflected directly from the bed's surface and exiting the reactor. At the same time, light that penetrated deep into the bed was more easily absorbed by the surrounding particles when reflected from the surface of the particles, creating a light trapping effect, and increasing the light absorptivity. The total absorptivity of the fluidized bed at different times is shown in Fig. 3. At the initial moment, that is, under fixed bed conditions, the light absorption rate of the bed is 87.14%. When the particles enter the fluidized state, the light absorption rate increases. At any time during the fluidization, the total absorptivity is higher than that of the fixed bed. The average absorptivity within 0.2–2 s was 88.17%, which is 1.18% higher than that in fixed bed. The properties of the particles remained unchanged in the fluidized bed. Although the particles themselves had high absorptivity, their movement allowed light to penetrate deeper, further enhancing overall light absorption. This emphasizes the advantages of the PFBR compared to fixed beds in terms of light absorption.

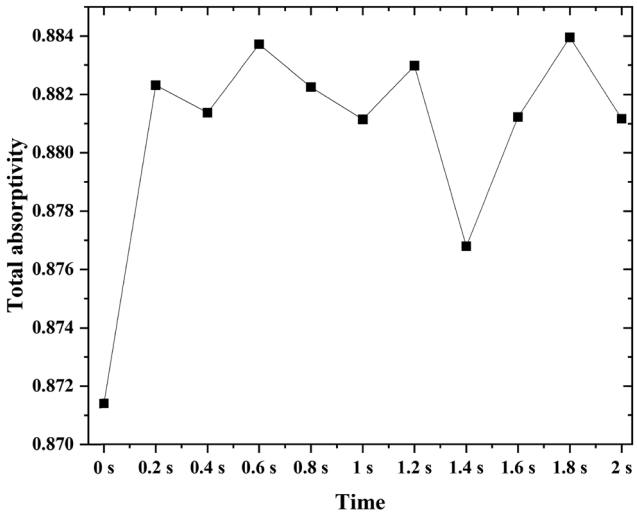

Fig. 3 The total absorptivity of the fluidized bed at different times with the gas flow set at 10 sccm and particle absorptivity 0.95; note that at time 0 s, the bed is in the fixed (non-fluidized) state.

The effects of other parameters on the light absorption of the fluidized bed were also considered. Fig. 4a illustrates the total light absorptivity of the fluidized bed for particles with varying absorptivity, along with the corresponding enhancement compared to the fixed bed. With the decrease in the particle's absorptivity, the total light absorbed by the fluidized bed and fixed bed decreased. However, when the absorptivity of the particles was low, the enhancement of light absorption in the fluidized bed was more obvious than that in the fixed bed. At a particle absorptivity of 0.5, the fluidized bed exhibited a 12.87% enhancement in light absorption compared to the fixed bed, demonstrating that the PFBR is particularly effective for photocatalysts or photothermal catalysts with low intrinsic absorptivity by significantly improving their overall

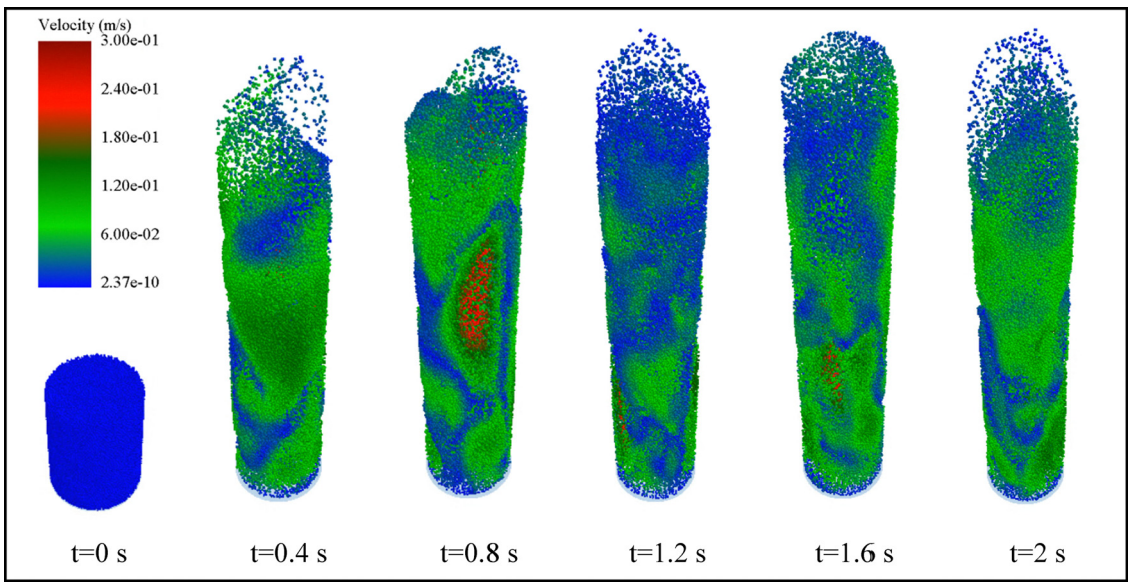

Fig. 2 Changes of particle flow state over time (10 sccm CO_2 flow rate, 10 mg carbon with 110 μm diameter).

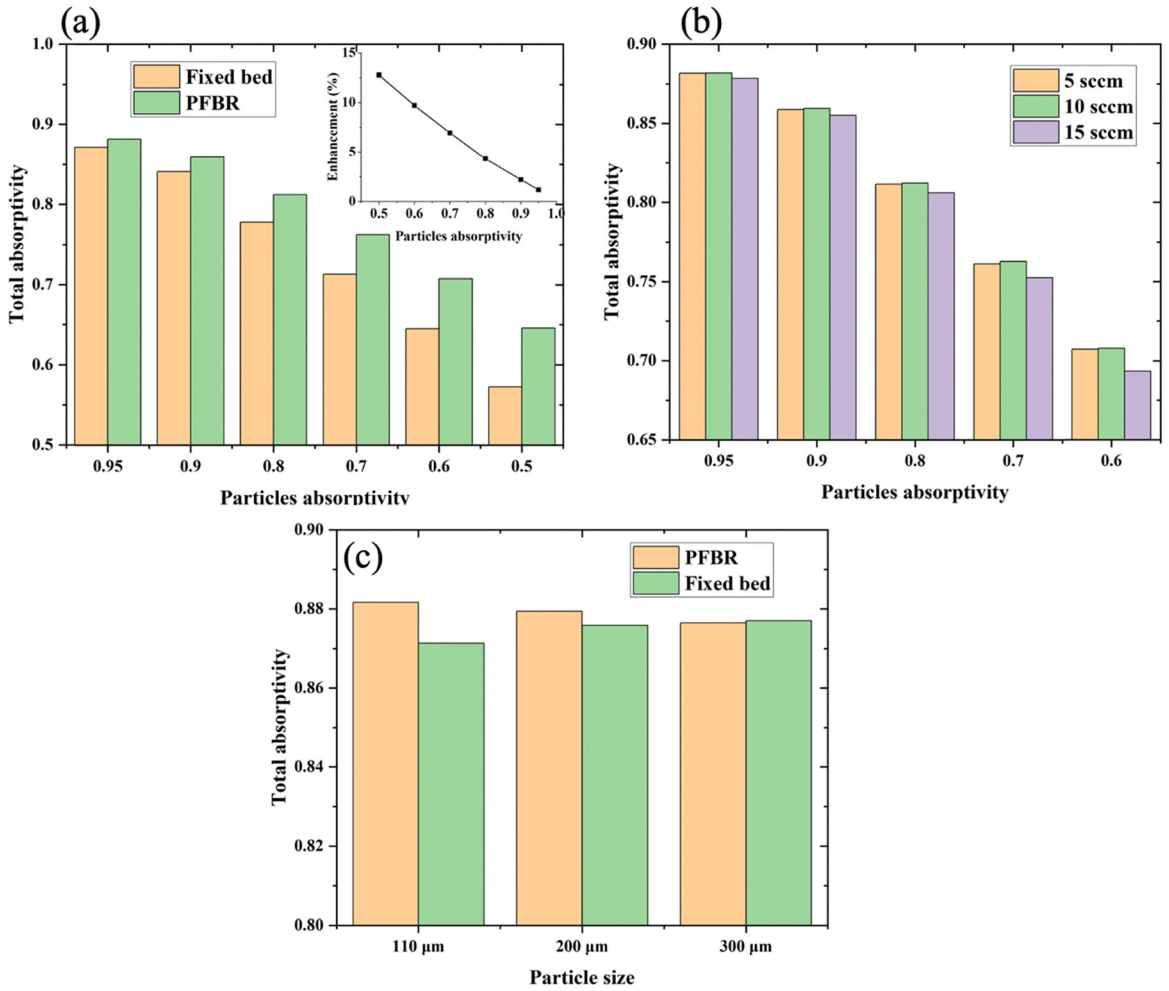

Fig. 4 Comparison of total absorptivity between fluidized bed and fixed bed configurations. (a) Total absorptivity at different particle absorptivities; the inset shows the corresponding enhancement compared to the fixed bed. (b) Total absorptivity at varying gas flow rates. (c) Total absorptivity at different particle sizes (gas flow rate: 5 sccm; particle absorptivity: 0.95). In all cases, the reported absorptivity values represent the time-averaged results over the interval from 0.2 s to 2 s.

light utilization. Fig. 4(b) shows the total absorptivity of the PFBR at different gas flow rates. When the gas flow rate increased from 5 sccm to 10 sccm, the total light absorption rate of the fluidized bed increased slightly, but it did not vary significantly across different particle absorptivity. However, as the gas flow rate was further increased to 15 sccm, the total absorption rate decreased, especially at low particle absorptivity. When the gas flow rate increased from 5 sccm to 10 sccm, particle spacing increased, allowing more light to penetrate the bed and enhancing light absorption. However, at 15 sccm, the bed height increased further, causing more direct light penetration and subsequent absorption losses. Therefore, selecting an optimal gas flow rate in the PFBR is crucial to maximize light interaction with particles and minimize losses. Fig. 4(c) compares the total absorptivity of the PFBR and the fixed bed using different particle sizes at a constant gas flow rate. As particle diameter increased, the corresponding increase in mass made it harder for particles to be fluidized at a constant gas flow rate. Consequently, smaller particles achieved greater dispersion in the PFBR, increasing interparticle spacing and allowing deeper light penetration into the bed. As shown in Fig. 4(c), smaller particles in the PFBR exhibited higher light absorption due to better dispersion and increased interparticle spacing. In contrast, in the fixed bed, larger particles led to greater light absorption. This is attributed to increased surface roughness and deeper interstitial textures, which promote multiple reflections and enhanced absorption. However, for 300 μm particles, limited fluidization at the set gas flow rate resulted in minimal difference between the fixed and fluidized bed absorption performance. Therefore, higher gas flow rates are necessary to effectively fluidize larger particles and increase interparticle spacing, thereby enhancing total light absorption. For a practical PFBR design, smaller particles are advantageous as they promote better light penetration and require lower gas flow rates. Optimizing the gas flow is essential, as both excessively high and low flow rates can negatively impact light absorption. While a PFBR significantly improves the light absorption of low-absorptivity particles, substantial losses still occur due to reflection.

Thus, selecting particles with intrinsically high absorptivity is crucial for maximizing overall light utilization.

3.2 Experimental performance

The experimental performance of the reverse-Boudouard reaction across various light intensities and gas flow rates in both PFBR and fixed bed configurations is shown in Fig. 5. The findings demonstrate that the carbon monoxide (CO) production rate, as anticipated, increased with increasing light intensity. At low inlet flow rates, the fluidized bed exhibited significantly better performance than the fixed bed. Notably, performance could be improved by as much as 1.6 times when the light intensity reached 48.4 W cm^{-2} and the gas flow rate was maintained at 5 sccm. When the CO_2 flow rate was set at 10 sccm and light intensity was 32.66 W cm^{-2}, the performance gap between the fluidized bed and fixed bed was relatively small. However, the fluidized bed still outperformed the fixed bed at high light intensities. In contrast, at a flow rate of 15 sccm, the CO production rate in the fixed bed was greater than that in the fluidized bed. This difference is attributed to the increased bed height at higher CO_2 flow rates. As the height of the fluidized bed increased while the diameter of the incident light beam remained fixed at the level of the original fixed bed, a considerable portion of particles was elevated to above the illuminated zone, thereby receiving insufficient light exposure. For future applications, it is essential to optimize the gas flow rate to maintain particle motion within an effective range, thereby enhancing reaction conversion efficiency. The photon-to-yield efficiencies of the solar reverse Boudouard reaction were 0.04% for the PFBR and 0.02% for the fixed bed, under conditions of 5 sccm and 48.41 W cm^{-2}. In the PFBR, light penetrated deeper into the bed, and the movement of particles allowed for a wider range of particles to absorb light. This means that the photon-to-yield efficiency can be improved using the PFBR. Currently, the photon-to-yield efficiency of carbon photocatalysis is low and comparable to that of other photocatalysts (see Table S1, ESI†). Further efforts are necessary to enhance the photon-to-yield efficiency in the PFBR, as will be discussed in the Conclusions and perspectives section.

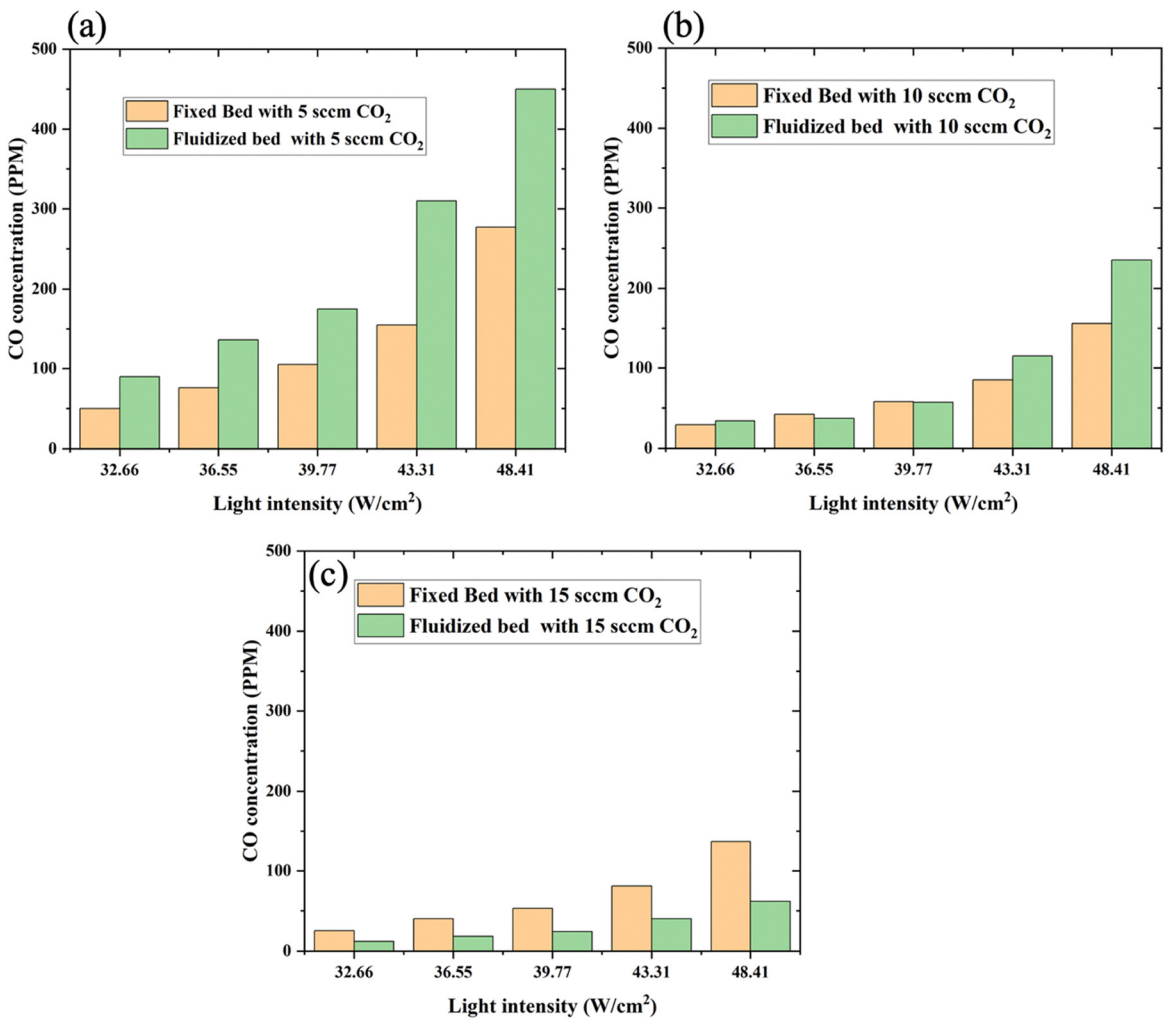

Fig. 5 Experimental performance of the reverse Boudouard reaction under varying gas flow rates and light intensities in both the PFBR and fixed bed configurations: (a) at 5 sccm, (b) at 10 sccm, and (c) at 15 sccm.

Additional experiments were conducted to assess the apparent activation energies (E_a) of the reverse Boudouard process under both light and dark conditions within the PFBR. At the same reaction temperature, CO generation was significantly enhanced under light-assisted conditions compared to dark conditions (Fig. 6a). The light-assisted reaction exhibited a significantly lower activation energy, with an E_a value of 31.5 kJ mol^{-1} for the light-assisted reaction and 88.3 kJ mol^{-1} for the thermal reaction (Fig. 6b). These results confirm the crucial role of light in the carbon photochemical process. Previous research by our group has also demonstrated that the light-driven reaction follows a different mechanism than the thermal reaction observed in fixed beds.[48] The reaction performance under varying light intensities at reactor temperatures of 500 °C and 600 °C is depicted in Fig. 6(c) and (d). In the absence of light irradiation, the catalytic temperature remains lower than the reactor temperature. However, as the light intensity increases, both the catalytic temperature and the reaction rate increase. Notably, the enhancement of the reaction rate is particularly sensitive to changes in light intensity.

The carbon samples before and after the reverse-Boudouard reaction in both the PFBR and fixed bed reactor were characterized using TEM, PXRD, and XPS to determine if there were any changes in the carbon structure after the reaction in either reactor configuration. Carbon particles are comprised of an assembly of primary aggregates. The carbon particles maintained a semi-spherical morphology with an average particle size smaller than 100 nm, as shown in Fig. S2 (ESI†). PXRD analysis of the carbon samples revealed two main broad peaks, indicating a poorly ordered graphitic structure, along with a slightly asymmetric displacement on the (100) crystallographic plane at 44.5° as shown in Fig. S3 (ESI†). The diffraction pattern also preserved the (002) plane at 26.6° after light irradiation. This suggests that the carbon structure is resilient to deleterious photodegradation during CO production and is simply consumed in the carbon photochemistry process. XPS analysis further confirmed that the structure and surface chemistry of the carbon remained essentially unchanged after the reaction (see Fig. S4, S5 and Table S2, ESI†). The C 1s spectra were nearly identical for the carbon samples before and after the reaction, with similar elemental analytical quantification observed in both cases. Carbon samples after the reaction in the PFBR showed less elemental oxygen, confirming maximized light penetration and interaction with most of the fluidized carbon.

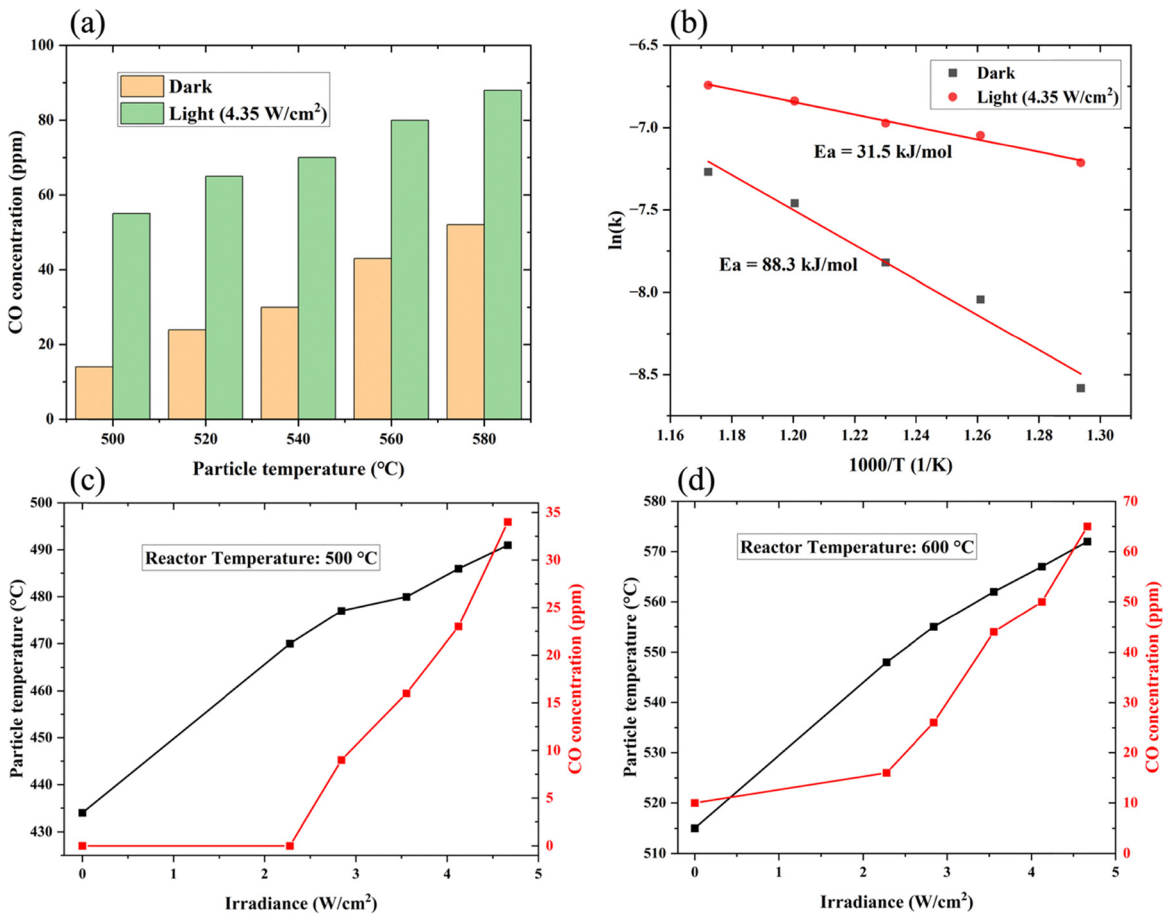

Fig. 6 Experimental performance of the reverse Boudouard reaction within the PFBR. (a) CO production rate under dark and illuminated conditions at various particle temperatures. (b) Apparent activation energy under dark and illuminated conditions. (c) Particle temperature and CO production rate at different light intensities at a reactor temperature of 500 °C. (d) Particle temperature and CO production rate at different light intensities at a reactor temperature of 600 °C.

4. Conclusions and perspectives

In this work, we explored the light absorption characteristics of PFBR for the first time by combining CFD-DEM simulations and ray tracing. Compared to a fixed bed, the fluidized bed significantly enhanced light absorption, with the overall absorption improvement being more pronounced as particle absorptivity decreased. For instance, when particle absorptivity was 0.5, the total light absorption rate in PFBR increased by 12.87% compared to that of the fixed bed. Additionally, small particles resulted in a more effective PFBR light absorption enhancement. The gas flow rate had to be optimized to ensure that particles maintained complete contact with the light, thereby maximizing absorption. Experimental results from the solar reverse Boudouard reaction conducted in both PFBR and fixed bed configurations demonstrated that gas flow not only influenced particle movement but also significantly affected reaction performance. Low gas flow rates enhanced the performance of the PFBR, which achieved double the photon-to-yield efficiency of the fixed bed. Furthermore, a comparison of thermal and photo-assisted reactions confirmed that light is a crucial factor in improving the performance of the reverse Boudouard reaction. The findings provide valuable insights for the future design of energy-efficient, cost-effective, and scalable PFBR systems, which could play a key role in the sustainable synthesis of chemicals and fuels.

Work in progress focuses on optimizing the opto-chemical engineering of light and particle interactions in the PFBR to further elevate PFBR performance. For example, implementing 360° light irradiation ensures that photocatalysts within the reactor receive uniform light and temperature, minimizing inefficiencies caused by shadowing and allowing for a more consistent reaction rate. Previous studies have demonstrated that red light can significantly enhance reactivity compared to other wavelengths. Building on this, reactor performance can be further improved by surrounding the reaction tube with red LED light, ensuring efficient irradiation. The integration of continuous LED irradiation, powered by batteries charged with green electricity from sustainable wind and solar sources, enables PFBRs to operate independently of natural light cycles and cloud fluctuations. This makes these systems highly adaptable to industrial needs, maintaining steady reaction kinetics while enhancing overall reactor efficiency. Scaling up PFBRs by an order of magnitude is crucial for advancing to the next technology readiness level, transitioning PFBRs from laboratory-scale proof-of-concept designs to commercially viable systems. The reverse Boudouard reaction consumes carbon feedstock throughout its operation; thus, to ensure long-term efficiency, a feeding system is necessary to maintain a stable particle volume. Additionally, impurities such as ash are generated during the reaction, and these small particles can be carried out of the reactor by the gas stream. To address this, a separator at the reactor outlet is essential for efficiently removing ash and other impurities. Additionally, expanding the application of PFBR technology to other photocatalysts and photocatalytic reactions will demonstrate its versatility, confirming PFBRs as a universally applicable solution in the realm of green chemistry. When integrated with current CCUS (carbon capture, utilization, and storage) technology, the collected CO_2 can be efficiently converted into valuable products through the reverse Boudouard reaction or hydrogenation processes. Additionally, using solar energy as the primary energy input eliminates the need for traditional energy sources, further contributing to a reduction in CO_2 emissions. Together, these advancements in PFBR design promise to propel sustainable carbon photochemistry toward new frontiers, opening pathways for broader industrial adoption and meaningful reduction in carbon footprints.

Data availability

The data that support the findings of this study are available from the corresponding author upon reasonable request.

Conflicts of interest

The author declares no competing interests.

Acknowledgements

The Solar Fuels Group (**https://www.solarfuels.utoronto.ca**) is grateful for the financial support from the Natural Sciences and Engineering Research Council of Canada and Hydrofuel Canada Inc. H. W. acknowledges the financial support from the China Scholarship Council (202306320315). H. W. and A. G. want to especially thank John Ford, Ahmed Bobat and David Heath from the machine shop at the University of Toronto for the fantastic work building the reactors and holders used in this project. All authors acknowledge the professional proof-reading and valuable discussions with Loki Peper.

References

1 D. Welsby, J. Price, S. Pye and P. Ekins, *Nature*, 2021, **597**, 230–234.
2 L. Noureen, Q. Wang, M. Humayun, W. A. Shah, Q. Xu and X. Wang, *Environ. Res.*, 2023, **219**, 115084.
3 Z. Zhang, C. Mao, D. M. Meira, P. N. Duchesne, A. A. Tountas, Z. Li, C. Qiu, S. Tang, R. Song and X. Ding, *Nat. Commun.*, 2022, **13**, 1512.
4 J. Sun, W. Sun, L. Wang and G. A. Ozin, *Acc. Mater. Res.*, 2022, **3**, 1260–1271.
5 M. Cai, Z. Wu, Z. Li, L. Wang, W. Sun, A. A. Tountas, C. Li, S. Wang, K. Feng, A.-B. Xu, S. Tang, A. Tavasoli, M. Peng, W. Liu, A. S. Helmy, L. He, G. A. Ozin and X. Zhang, *Nat. Energy*, 2021, **6**, 807–814.
6 S. Lin, H. Huang, T. Ma and Y. Zhang, *Adv. Sci.*, 2021, **8**, 2002458.
7 J. Guo, P. N. Duchesne, L. Wang, R. Song, M. Xia, U. Ulmer, W. Sun, Y. Dong, J. Y. Y. Loh, N. P. Kherani, J. Du, B. Zhu, W. Huang, S. Zhang and G. A. Ozin, *ACS Catal.*, 2020, **10**, 13668–13681.

8 X. Liu, Z. Mu, C. Sun, H. Shi, X. Meng, P. Li, Y. Ling, B. Cheng, Y. Xuan and Y. Ding, *Fuel*, 2022, **310**, 122441.
9 W. K. Fan and M. Tahir, *Chem. Eng. J.*, 2022, **427**, 131617.
10 Z. Wang, Z. Yang, R. Fang, Y. Yan, J. Ran and L. Zhang, *Chem. Eng. J.*, 2022, **429**, 132322.
11 C. G. Thomson, A.-L. Lee and F. Vilela, *Beilstein J. Org. Chem.*, 2020, **16**, 1495–1549.
12 O. Ola, M. Maroto-Valer, D. Liu, S. Mackintosh, C.-W. Lee and J. C. S. Wu, *Appl. Catal., B*, 2012, **126**, 172–179.
13 L. Li, W. Ouyang, Z. Zheng, K. Ye, Y. Guo, Y. Qin, Z. Wu, Z. Lin, T. Wang and S. Zhang, *Chin. J. Catal.*, 2022, **43**, 1258–1266.
14 J. Zhao, Q. Yang, R. Shi, G. I. N. Waterhouse, X. Zhang, L.-Z. Wu, C.-H. Tung and T. Zhang, *NPG Asia Mater.*, 2020, **12**, 5.
15 E. T. Kho, S. Jantarang, Z. Zheng, J. Scott and R. Amal, *Engineering*, 2017, **3**, 393–401.
16 X. Yu, L. Yang, Y. Xuan, X. L. Liu and K. Zhang, *Nano Energy*, 2021, **84**, 105953.
17 M. Tahir and N. S. Amin, *Appl. Catal., A*, 2013, **467**, 483–496.
18 M. Tahir and N. A. S. Amin, *Int. J. Hydrogen Energy*, 2017, **42**, 15507–15522.
19 S. Bhatta, D. Nagassou, S. Mohsenian and J. P. Trelles, *Sol. Energy*, 2019, **178**, 201–214.
20 X. E. Cao, Y. Kaminer, T. Hong, P. Schein, T. Liu, T. Hanrath and D. Erickson, *iScience*, 2020, **23**, 101856.
21 V. Madadi Avargani and S. Zendehboudi, *Energy Convers. Manage.*, 2023, **276**, 116539.
22 Z. Mu, X. Liu, C. Song, N. Sun, C. Tian and Y. Xuan, *Next Energy*, 2023, **1**, 100051.
23 P. Kant, S. Liang, M. Rubin, G. A. Ozin and R. Dittmeyer, *Joule*, 2023, **7**, 1347–1362.
24 S. Wang, K. Luo and J. Fan, *Chem. Eng. Sci.*, 2020, **217**, 115550.
25 M. Suárez-Almeida, A. Gómez-Barea, A. F. Ghoniem and C. Pfeifer, *Chem. Eng. J.*, 2021, **406**, 126665.
26 S. Wang and Y. Shen, *Renewable Energy*, 2020, **159**, 1146–1164.
27 S. Tong, B. Miao, W. Zhang, L. Zhang and S. H. Chan, *Energy Convers. Manage.*, 2023, **297**, 117719.
28 D. Torres, S. De Llobet, J. Pinilla, M. Lázaro, I. Suelves and R. Moliner, *J. Nat. Gas Chem.*, 2012, **21**, 367–373.
29 K. R. Parmar, K. Pant and S. Roy, *Energy Convers. Manage.*, 2021, **232**, 113893.
30 L. Pang, Y. Shao, W. Zhong and H. Liu, *Proc. Combust. Inst.*, 2021, **38**, 4121–4129.
31 Y. Cui, X. Liu and W. Zhong, *Energy Fuels*, 2020, **34**, 4977–4992.
32 R. J. Braham and A. T. Harris, *Phys. Chem. Chem. Phys.*, 2013, **15**, 12373–12385.
33 H.-Y. Ren, B.-F. Liu, J. Ding, G.-J. Xie, L. Zhao, D.-F. Xing, W.-Q. Guo and N.-Q. Ren, *RSC Adv.*, 2012, **2**, 5531–5535.
34 K. Reilly, F. Taghipour and D. P. Wilkinson, *Energy Procedia*, 2012, **29**, 513–521.
35 D. Mateo, J. L. Cerrillo, S. Durini and J. Gascon, *Chem. Soc. Rev.*, 2021, **50**, 2173–2210.
36 D. Dragomir and L. Druga, *Mater. Sci. Eng., A*, 2001, **302**, 115–119.
37 A. Di Renzo, F. Scala and S. Heinrich, *Processes*, 2021, **9**, 639.
38 H. Yuansheng and S. Mengshu, *Energy*, 2021, **220**, 119711.
39 C. Tregambi, C. Bevilacqua, M. Troiano, R. Solimene and P. Salatino, *Chem. Eng. J.*, 2020, **398**, 125702.
40 S. Fang, M. Rahaman, J. Bharti, E. Reisner, M. Robert, G. A. Ozin and Y. H. Hu, *Nat. Rev. Methods Primers*, 2023, **3**, 61.
41 S. Shoji, X. Peng, A. Yamaguchi, R. Watanabe, C. Fukuhara, Y. Cho, T. Yamamoto, S. Matsumura, M.-W. Yu and S. Ishii, *Nat. Catal.*, 2020, **3**, 148–153.
42 G. J. Rincón and E. J. La Motta, *Heliyon*, 2019, **5**, e01966.
43 K. Reilly, D. P. Wilkinson and F. Taghipour, *Appl. Energy*, 2018, **222**, 423–436.
44 K. Reilly, B. Fang, F. Taghipour and D. P. Wilkinson, *J. Catal.*, 2017, **353**, 63–73.
45 X. Lu, J. Z. Y. Tan and M. M. Maroto-Valer, *Ind. Eng. Chem. Res.*, 2022, **61**, 3123–3136.
46 C. J. Bueno-Alejo, J. L. Hueso, R. Mallada, I. Julian and J. Santamaria, *Chem. Eng. J.*, 2019, **358**, 1363–1370.
47 C. Gusmão, P. H. Palharim, L. A. Diniz, G. C. de Assis, T. de Carvalho e Souza, B. Ramos and A. C. S. C. Teixeira, *Ind. Eng. Chem. Res.*, 2024, **63**, 14967–14982.
48 C. J. V. Pérez, J. M. Restrepo-Florez, J. Ye, N. T. Nguyen, A. A. Tountas, R. Song, C. Mao, A. Wang, A. Gouda, S. J. E. Corapi and E. Science, *Energy Environ. Sci.*, 2023, **16**, 6155–6167.
49 M. Chen, M. Liu and Y. Tang, *Int. J. Chem. React. Eng.*, 2019, **17**, 20180254.
50 M. Nouri, G. Rahpaima, M. M. Nejad and M. Imani, *Comput. Chem. Eng.*, 2018, **108**, 1–10.
51 M. Chen, Z. Chen, M. Gong, Y. Tang and M. Liu, *Particuology*, 2021, **57**, 112–126.
52 A. Rastgaran, H. Fatoorehchi, N. Khallaghi, A. Larimi and T. N. Borhani, *Carbon Capture Sci. Technol.*, 2023, **8**, 100118.
53 M. J. A. de Munck, E. A. J. F. Peters and J. A. M. Kuipers, *Chem. Eng. Sci.*, 2024, **291**, 119922.
54 S. Wang, K. Luo, C. Hu, J. Lin and J. Fan, *Chem. Eng. Sci.*, 2019, **197**, 280–295.
55 D. Liu and B. van Wachem, *Powder Technol.*, 2019, **343**, 145–158.
56 S. D. A. Zondag, J. H. A. Schuurmans, A. Chaudhuri, R. P. L. Visser, C. Soares, N. Padoin, K. P. L. Kuijpers, M. Dorbec, J. van der Schaaf and T. Noël, *Nat. Chem. Eng.*, 2024, **1**, 462–471.
57 S. Aboudaoud, S. Touzani, S. Abderafi and A. Cheddadi, *J. Appl. Fluid Mech.*, 2023, **16**, 1778–1791.
58 S. Hu, L. Vo, D. Monteiro, S. Bodnar, P. Prince and C. A. Koh, *Langmuir*, 2021, **37**, 1651–1661.
59 D. Gidaspow, *Multiphase flow and fluidization: continuum and kinetic theory descriptions*, Academic press, 1994.
60 Y. Gao, M. Wang, A. Raheem, F. Wang, J. Wei, D. Xu, X. Song, W. Bao, A. Huang, S. Zhang and H. Zhang, *ACS Omega*, 2023, **8**, 31620–31631.
61 M. Keller and A. Sharma, *Chem. Eng. J.*, 2022, **431**, 134127.
62 M. Asadullah, *Renewable Sustainable Energy Rev.*, 2014, **29**, 201–215.